Title

Co-Folding of a FliF-FliG Split Domain Forms the Basis of the MS:C Ring Interface within the Bacterial Flagellar Motor

Journal

Structure, 25(2)

ISSN

1359-0278

Authors

Lynch, Michael J
Levenson, Robert
Kim, Eun A
et al.

Publication Date

2017-02-01

DOI

10.1016/j.str.2016.12.006

Peer reviewed

Article

Structure

Co-Folding of a FliF-FliG Split Domain Forms the Basis of the MS:C Ring Interface within the Bacterial Flagellar Motor

Graphical Abstract

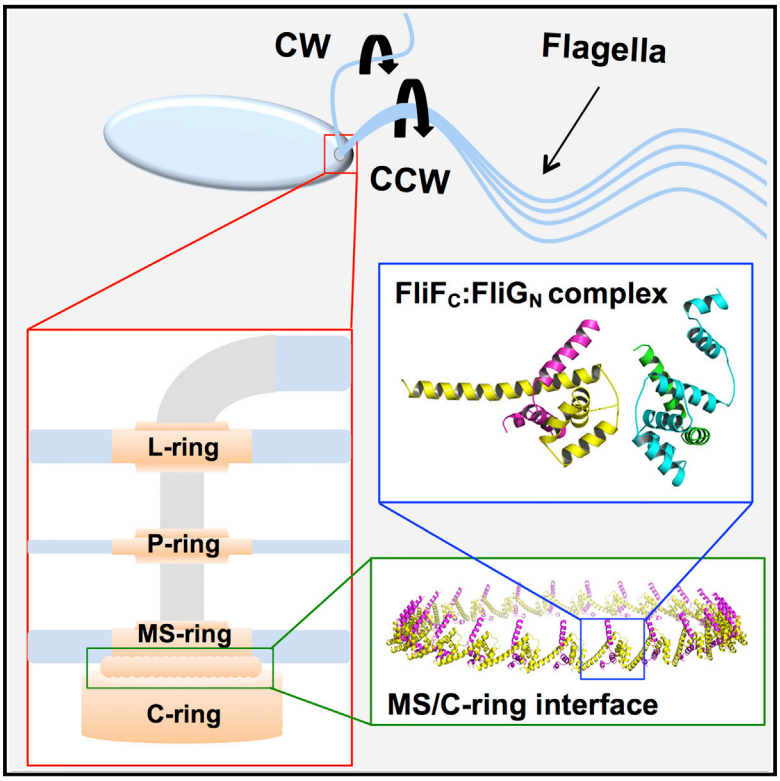

Authors

Michael J. Lynch, Robert Levenson, Eun A Kim, Ria Sircar, David F. Blair, Frederick W. Dahlquist, Brian R. Crane

Correspondence

bc69@cornell.edu

In Brief

FliF and FliG comprise the MS ring and upper C ring of the bacterial flagellar motor. Lynch et al. use X-ray crystallography, SAXS, NMR, and in vivo studies to reveal how FliF:FliG fold into a single domain, whose topology is found elsewhere in FliG, and generate an updated model of the upper flagellar rotor.

Highlights

- FliF$_C$:FliG$_N$ fold together to produce a topology that repeats throughout FliG
- FliF$_C$:FliG$_N$ interact through hydrophobic contacts critical for motor function
- FliF:FliG 1:1 stoichiometry produces an MS/C-ring interface with ~C$_{25}$-fold symmetry

Accession Numbers

5TDY

Lynch et al., 2017, Structure *25*, 317–328
February 7, 2017
http://dx.doi.org/10.1016/j.str.2016.12.006

Structure
Article

Co-Folding of a FliF-FliG Split Domain Forms the Basis of the MS:C Ring Interface within the Bacterial Flagellar Motor

Michael J. Lynch,[1] Robert Levenson,[2] Eun A Kim,[3] Ria Sircar,[1] David F. Blair,[3] Frederick W. Dahlquist,[2] and Brian R. Crane[1,4,*]
[1]Department of Chemistry and Chemical Biology, Cornell University, Ithaca, NY 14853, USA
[2]Department of Chemistry and Biochemistry, University of California Santa Barbara, Santa Barbara, CA 93106-9510, USA
[3]Department of Biology, University of Utah, Salt Lake City, UT 84112, USA
[4]Lead Contact
*Correspondence: bc69@cornell.edu
http://dx.doi.org/10.1016/j.str.2016.12.006

SUMMARY

The interface between the membrane (MS) and cytoplasmic (C) rings of the bacterial flagellar motor couples torque generation to rotation within the membrane. The structure of the C-terminal helices of the integral membrane protein FliF ($FliF_C$) bound to the N terminal domain of the switch complex protein FliG ($FliG_N$) reveals that $FliG_N$ folds around $FliF_C$ to produce a topology that closely resembles both the middle and C-terminal domains of FliG. The interface is consistent with solution-state nuclear magnetic resonance, small-angle X-ray scattering, in vivo interaction studies, and cellular motility assays. Co-folding with $FliF_C$ induces substantial conformational changes in $FliG_N$ and suggests that FliF and FliG have the same stoichiometry within the rotor. Modeling the $FliF_C$:$FliG_N$ complex into cryo-electron microscopy rotor density updates the architecture of the middle and upper switch complex and shows how domain shuffling of a conserved interaction module anchors the cytoplasmic rotor to the membrane.

INTRODUCTION

The bacterial flagellar motor is the principal organelle that enables motile bacteria to move within their environment. The motor can be divided into three major components: (1) the filament, which serves as the propeller of the motor, (2) the hook, a flexible adaptor between the filament and cell body, and (3) the basal body, which generates torque and induces flagellar rotation switching. The basal body (Figure 1) is composed of a series of transmembrane rings that enclose a central rod. Powered by the proton or sodium gradient that spans the inner membrane, torque is generated by interactions between the membrane-embedded ion channels and the switch complex located in the cytosolic space (Berg, 2003; Minamino et al., 2008; Minamino and Imada, 2015; Sowa and Berry, 2008; Chen et al., 2011). The switch complex forms the C ring and is composed of the proteins FliG, FliM, and FliN (or FliY) (Figure 1). The switch complex rotates either counterclockwise (CCW) or clockwise (CW) and in doing so dictates whether the cell swims smoothly or tumbles in solution. Interaction of the switch complex with the phosphorylated form of the response regulator CheY causes switching of rotation direction (Berg, 2003; Sowa and Berry, 2008).

A prerequisite for motor operation and assembly during the early stages of flagellar biosynthesis is the correct positioning of the switch complex relative to the MS ring (Macnab, 2003; Grünenfelder et al., 2003; Chevance and Hughes, 2008; Minamino et al., 2008; Minamino and Imada, 2015). Located in the inner membrane and composed of approximately 25 copies of a single transmembrane protein, FliF, the MS ring is the first circular structure to form during flagellar assembly (Figure 1) (Macnab, 2003; Chevance and Hughes, 2008; Sowa and Berry, 2008). The MS ring adheres to the switch complex through interactions mediated between the C-terminal tail of FliF ($FliF_C$) and the N-terminal region of FliG ($FliG_N$) (Francis et al., 1992; Thomas et al., 2001; Brown et al., 2002; Grünenfelder et al., 2003). Electron microscopy (EM), site-directed alanine-scanning mutagenesis, and fusion/deletion studies have revealed that these two proteins directly interact with one another in a 1:1 stoichiometric ratio (Thomas et al., 1999, 2001, 2006; Ogawa et al., 2015). The structure of FliG has been determined for the full-length protein (Lee et al., 2010) and the individual domains (Brown et al., 2002; Minamino et al., 2011), alone and in complex with domains of FliM (Paul et al., 2011; Vartanian et al., 2012; Lam et al., 2013; Sircar et al., 2015). FliF is an integral membrane protein with extensive periplasmic domains homologous to the injectosome SctJ/D proteins and the sporulation factors SpoIIIAG/H (Bergeron, 2016). FliG and FliF orthologs are found in essentially all flagellated (and some non-flagellated) bacteria, and thus this interaction can be considered a universal contact made in bacterial flagella (Levenson et al., 2012; Bergeron, 2016).

To characterize the interaction between $FliF_C$ and $FliG_N$, Levenson et al. (2012) employed tryptophan fluorescence and ^{1}H-^{15}N transverse relaxation optimized spectroscopy (TROSY)-heteronuclear single quantum coherence (HSQC) nuclear magnetic resonance (NMR) spectroscopy to map the binding surface of *Thermotoga maritima* $FliF_C$ on $FliG_N$. The K_d between $FliG_N$ and $FliF_C$ was measured in the low nanomolar range (<40 nM), and $FliF_C$ binding caused chemical shift perturbations

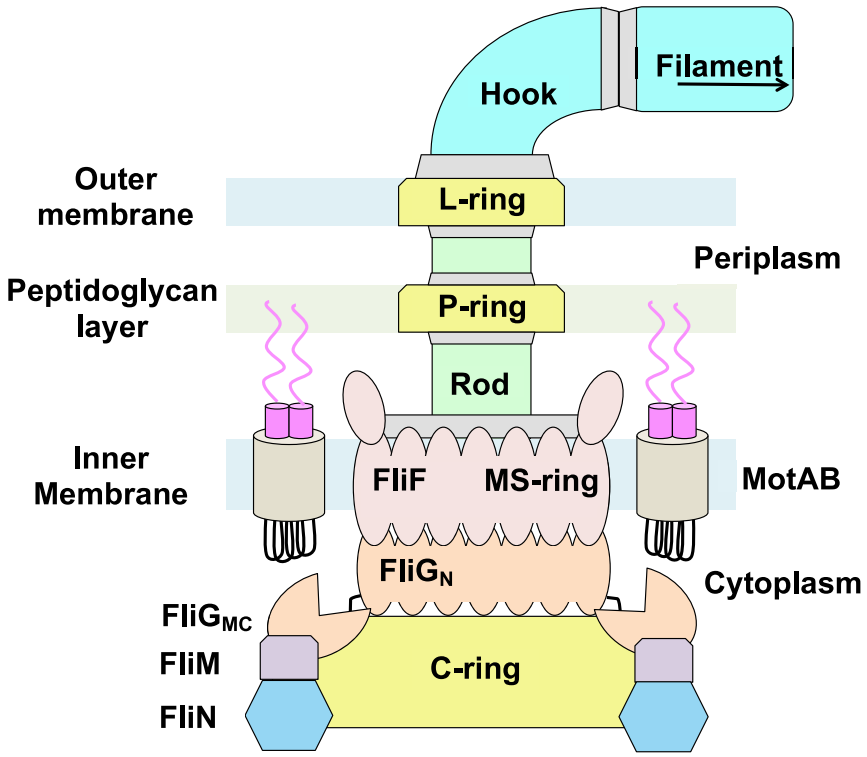

Figure 1. Schematic Diagram of the Bacterial Flagellar Motor

of backbone resonances across the entirety of FliG$_N$. As a whole, the data suggested that the FliG$_N$ domain orders as a result of FliF$_C$ binding, an effect consistent with multi-angle light scattering experiments that demonstrated the dissociation of FliG homodimers to form mixed FliF$_C$:FliG heterodimers upon FliF$_C$ addition (Levenson et al., 2012). A strong interaction between FliF$_C$ and FliG$_N$ agrees well with previous observations made when purifying intact flagellar motors from *Salmonella* cells. Intact basal bodies readily lose the FliM and FliN regions of the C ring; however, very low pH is required to induce dissociation of the FliF:FliG interface, owing to the unique strength of the interaction (Francis et al., 1994). More recently, a similar interaction between FliF and FliG was reconstituted with a soluble full-length form of FliF from a marine *Vibro* species (Ogawa et al., 2015).

Herein, we report the crystal structure of a complex between FliF$_{495-532}$ (FliF$_C$) and FliG$_{1-98}$ (FliG$_N$). All three domains of full-length FliG have a strikingly similar topology when FliG$_N$ is bound to FliF$_C$. Indeed, FliG$_N$ folds around the FliF$_C$ helices and produces a structure similar to that of the FliG middle domain (FliG$_M$) and the FliG C-terminal domain (FliG$_C$) (Brown et al., 2002; Lee et al., 2010). Solution NMR, small-angle X-ray scattering (SAXS), and biochemical data are fully consistent with the structure and help differentiate between two alternative complexes found in the crystal lattice. The FliF$_C$:FliG$_N$ structure was then used to model the MS/C-ring interface in the context of cryo-EM density for whole *Salmonella* rotors (Thomas et al., 2006). An extended C-ring structure was generated taking into account previously placed FliG$_{MC}$:FliM$_M$ units (Sircar et al., 2015). Targeted crosslinking and motility assays of structure-guided variant proteins reveal the functional importance of the FliF$_C$:FliG$_N$ interaction.

RESULTS

Solution-State Properties of an Engineered FliF$_C$:FliG$_N$ Fusion Protein

FliF$_C$:FliG$_N$ (FliF$_C$(495–532):FliG$_N$(1–98) for crystallography and FliF$_C$(495–532):FliG$_N$(1–102) for NMR) were produced as chimeric fusion proteins to ensure a 1:1 component ratio (Figure S1). The constructs were engineered such that FliG and FliF are linked together via a sequence containing a His$_8$ tag bracketed by two tobacco etch virus (TEV) protease sites (or one TEV protease site between His$_8$ and FliG$_N$ for the NMR studies). ^{1}H-^{15}N TROSY-HSQC NMR spectroscopy was employed to evaluate the resulting complex before and after TEV proteolysis (Figure 2B). In addition, the cleaved complex was compared with that of ^{15}N-labeled FliG$_N$ incubated with a synthetic FliF$_C$ peptide corresponding to the identical sequence encoded by the fusion construct (Figure 2A) (Levenson et al., 2012) The ^{1}H-^{15}N TROSY-HSQC spectra of the FliF$_C$:FliG$_N$ fusion construct after TEV proteolysis (Figure 2A, red) is nearly identical to that of ^{15}N-labeled FliG$_N$ incubated with stoichiometric amounts of the corresponding FliF$_C$ peptide (Figure 2A, black). Thus, the cleaved fusion protein has a conformation similar to that of FliG$_N$ mixed with FliF$_C$. Similarly, there are little differences in the measured ^{1}H-^{15}N resonances before (black) and after (red) TEV proteolysis (Figure 2B), indicating that the intact and cleaved proteins are remarkably similar in organization. Resonances of isotopically labeled TEV-proteolyzed FliF$_{495-532}$:FliG$_{1-102}$ complex were assigned using standard 3D NMR techniques, yielding assignments for 93% of residues (Figure S2A). Cα chemical shift deviations from random coil values showed both FliF$_{495-532}$ and FliG$_{1-102}$ within the complex to be well folded, with α helical structure (Figure S2B). Overall, the data indicate the FliF$_C$:FliG$_N$ complex is the same whether produced as a fusion protein or as separate components and that the presence of a linker does not prevent complex assembly.

Solution-State Structure of the FliF$_C$:FliG$_N$ Complex by SAXS

SAXS was used to evaluate the FliF$_C$:FliG$_N$ solution-state structure. For these experiments, size-exclusion chromatography (SEC) was coupled to the SAXS measurements to separate different oligomeric or conformational states and limit contamination of soluble aggregates. The SEC chromatogram of the purified FliF$_C$:FliG$_N$ complex (Figure S3A) reveals a well-behaved protein complex. SAXS was measured for the area enclosed by the black dotted lines on the SEC chromatogram shown in Figure S3A. Kratky analysis of the scattering data (Figure S3B)

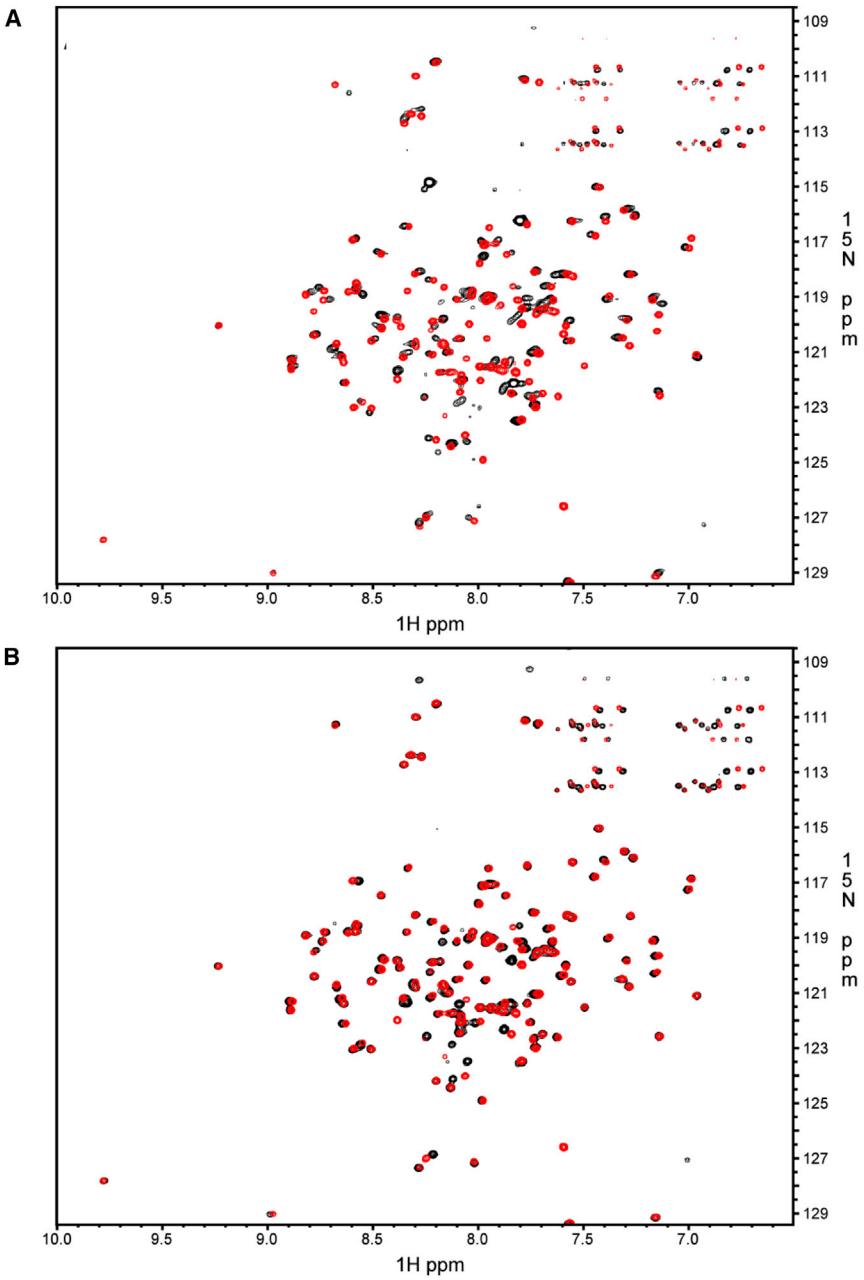

Figure 2. NMR Characterization of the $FliF_{495-532}$:$FliG_{1-102}$ Complex

(A) Black: TROSY-HSQC data of ^{15}N-labeled $FliG_{1-102}$ bound to unlabeled $FliF_{495-532}$ peptide. Red: TROSY-HSQC data of ^{15}N-labeled $FliF_{495-532}$:$FliG_{1-102}$ fusion protein after TEV proteolysis.

(B) Black: TROSY-HSQC data of ^{15}N-labeled $FliF_{495-532}$:$FliG_{1-102}$ fusion protein before TEV proteolysis. Red: TROSY-HSQC data of ^{15}N-labeled $FliF_{495-532}$:$FliG_{1-102}$ fusion protein after TEV proteolysis.

See also Figures S1, S2, and S6.

converges toward zero at high q values, characteristic of a globular protein complex (Lipfert and Doniach, 2007). Generation of a low-resolution de novo molecular envelope of the protein complex results in a globular envelope with an extended region (Figure S3B). Interestingly, there appears to be poor agreement between the envelope and the structure of $FliG_N$ from a full-length FliG structure determined from *Aquifex aeolicus* (Figure S3D; Lee et al., 2010). Either the binding of $FliF_C$ to $FliG_N$ produces a substantial conformational change in $FliG_N$ or the $FliF_C$ peptide is large enough to account for the unfilled area within the envelope. It is likely that FliF binding alters FliG, as the interaction converts FliG from a homodimer (FliG:FliG) to heterodimer (FliG:FliF) (Levenson et al., 2012). For more information regarding SAXS data acquisition and envelope generation, see Supplemental Experimental Procedures.

Crystal Structure of $FliF_C$:$FliG_N$ Complex

Crystals of the $FliF_C$:$FliG_N$ complex were grown by vapor diffusion at pH 7.5 (see Experimental Procedures). Attempts to determine the structure of $FliF_C$:$FliG_N$ by molecular replacement failed, therefore a selenomethionine (seMet) variant of the $FliF_C$:$FliG_N$ complex was crystallized (see Experimental Procedures). The seMet $FliF_C$:$FliG_N$ crystals diffracted to 2.6 Å resolution and yielded an initial single-wavelength anomalous diffraction phased map with a figure of merit of 0.341. A de novo model was built and refined into the map with excellent final agreement statistics (Table 1). The unit cell consisted of two heterodimers per asymmetric unit, with one dimer having an extended α helix toward the C-terminal portion of the FliG peptide, and the other having three segmented helices (Figure 3A). Although the two conformations of the last α helix in $FliG_N$ may indicate flexibility of this helix, the dimer with the extended α helix (Figure 3) agrees better with the SAXS envelopes and is thus presumed to represent the dominant solution-state structure (Figure S4C).

The $FliF_C$ terminal peptide forms two α helices connected by a short extended linker ($F_C\alpha1$ residues 497–514, and $F_C\alpha2$ 517–529, Figure 3B). $FliG_N$ is an all α-helical structure, similar to the all α-helical *T. maritima* $FliG_M$ and $FliG_C$ domains (Brown et al., 2002; Paul et al., 2011; Sircar et al., 2015), as well as the full-length FliG from *A. aeolicus* (Lee et al., 2010). $FliG_N$ consists of four helices, denoted $G_N\alpha1$-4 in Figure 3B (residues 6–19, 21–30, 33–45, and 51–87, respectively) where $G_N\alpha1$-3 form an ARM-like domain that is also present in $FliG_M$ and $FliG_C$ (Brown et al., 2002; Lee et al., 2010). Together with $F_C\alpha2$, $G_N\alpha1$-3 comprise a four-membered right-handed superhelix that has been well documented as a structural motif in other FliG structures (Brown et al., 2002; Lee et al., 2010; Paul et al., 2011)

Table 1. Data Collection and Refinement Statistics

	Wild-type $FliF_C$:$FliG_N$ Complex	Selenomethionine $FliF_C$:$FliG_N$ Complex
Wavelength (Å)	0.97700	0.97921
Synchrotron	CHESS[a]	APS[b]
Beamline	A1	24-ID-E
Space group	$P2_1$	$P2_1$
a, b, c (Å)	49.18, 59.33, 51.72	48.81, 59.24, 51.76
α, β, γ (°)	90.00, 115.59, 90.00	90.00, 115.76, 90.00
Resolution (Å)	50.0–2.10 (2.15–2.10)	50.0–2.60 (2.66–2.60)
R_{merge} (%)[c]	8.2	12.2
$R_{p.i.m.}$ (%)[c]	5.5 (21.8)	5.3 (15.8)
R_{meas} (%)[c]	9.9 (35.5)	13.3 (38.8)
$\langle I/\sigma(I)\rangle$	13.4 (3.2)	14.8 (7.0)
Completeness (%)	99.5 (99.6)	99.2 (99.5)
Multiplicity	3.1 (2.4)	6.0 (6.0)
Anomalous completeness (%)		98.1
Mosaicity	0.43–0.81	0.63–2.55
Total reflections	47,958	46, 599
Phaser FOM		0.341
Refinement		
Resolution (Å)		44.35–2.10 (2.18–2.10)
No. of unique reflections		15,618 (1,559)
Reflections used for R_{free}		1,556 (161)
R_{work}/R_{free} (%)		16.9 (17.4)/21.7 (23.7)
Clash score		4.70
No. of non-hydrogen atoms		2,263
Protein		2090 (260 residues)
Water		173
B factors (Å^2)		
Wilson		18.1
Average *B* factors		24.3
Protein		23.7
Water		31.8
RMSDs		
Bond lengths (Å)		0.007
Bond angles (°)		0.9
Ramachandran outliers (%)		0.4
Rotamer outliers (%)		1.3

Statistics for the highest-resolution shell are shown in parentheses.
[a]Cornell High Energy Synchrotron Source, Cornell University.
[b]Advanced Photon Source, Argonne National Lab.
[c]$R_i = \Sigma\Sigma_i\, |I_i - \langle I_i\rangle|/\Sigma\Sigma_i I_i$.

and is also found in the N-terminal cytoplasmic domain of the Mg^{2+} transporter MgtE (Hattori et al., 2007). We refer to these FliG super-helical domains as ARM-like motifs, following previous designations (Lee et al., 2010; Vartanian et al., 2012), although we note that these domains differ substantially from traditional ARM motifs in helix crossing angles and packing interactions (Andrade et al., 2001). $F_C\alpha1$ and $F_C\alpha2$ assume a hook-like structure that latches into the V-shaped cavity formed from the $G_N\alpha1$-3 superhelix and $G_N\alpha4$. In the unbound $FliG_N$ of *A. aeolicus* (Lee et al., 2010), $G_N\alpha1$-3 forms a similar superhelix but $G_N\alpha4$ is instead composed of two helices connected by a linker. Although similar in secondary structure, the unbound $FliG_N$ domain does not superimpose well with $FliG_N$ in complex with $FliF_C$ (Figure S4A). In the absence of $FliF_C$, $G_N\alpha4$ may be highly flexible, which would explain the difficulty in crystallizing unbound $FliG_N$.

$FliF_C$ and $FliG_N$ associate to form a shared hydrophobic core. Interacting regions of $FliF_C$ and $FliG_N$ mapped by NMR involve the burial of conserved hydrophobic residues on both $FliF_C$ and $FliG_N$ (Levenson et al., 2012). Similarly, the electrostatic potential at the molecular surface of $FliG_N$ reveals a hydrophobic, non-charged FliF binding region. The $FliF_C$:$FliG_N$ complex buries ~1,700 Å^2 of hydrophobic binding surface on the $FliF_C$ peptide and is stabilized at the periphery by charge complementarity (Figure S5). A nearly invariant tryptophan residue essential for the $FliF_C$:$FliG_N$ interaction (*T. maritima* FliF W527) (Thomas et al., 2001; Levenson et al., 2012) is tightly sequestered within a hydrophobic pocket formed from $G_N\alpha1$, $G_N\alpha4$, and $F_C\alpha2$ (Figure S5E).

From the extensive hydrophobic interactions, it appears as though $FliG_N$ folds around $FliF_C$. Surprisingly, the resulting topology matches that of the $FliG_M$ and $FliG_C$ domains (Figure 4A and 4B). The structure of the $FliF_C$:$FliG_N$ complex superimposes well with the tertiary structure of $FliG_M$ and $FliG_C$ from *T. maritima* (Figure 4; left, $FliG_M$ PDB: 3SOH; right, $FliG_C$ PDB: 1LKV), producing root-mean-square (RMS) values of 1.053 Å (40 residues) and 1.227 Å (63 residues), respectively (Paul et al., 2011; Brown et al., 2002). Superposition of the $FliF_C$:$FliG_N$ complex with the middle and C-terminal domains from *A. aeolicus* $FliG_{FL}$ results in a similar outcome (Figure S4) (Lee et al., 2010).

Mapping of the $FliF_C$:$FliG_N$ Interface by Paramagnetic Resonance Enhancement

To further investigate the solution-state structure of the $FliF_C$:$FliG_N$ complex, paramagnetic relaxation enhancement (PRE) experiments were carried out in which ^{1}H-^{15}N TROSY-HSQC NMR spectra were collected on a $FliF_{495-532}$ (E508C):$FliG_{1-102}$ (*Escherichia coli* FliF numbering) mutant that was conjugated to an MTSL nitroxide spin label. Proximity to the conjugated MTSL causes neighboring ^{15}N backbone nuclei to experience increased resonance peak broadening. Mapping of the maximally broadened residues in $FliG_N$ from the spin label on $F_C\alpha1$ produces a binding interface that is in excellent agreement with the crystal structure (Figure S6; Table S2). Notably, a small portion of the C-terminal tail of $G_N\alpha4$ also experiences a significant amount of resonance peak broadening with peak intensities 27%–65% compared with that observed in the protein after the MTSL label has been reduced to a spectrally inactive form by addition of ascorbic acid, despite these residues being relatively far removed from the spin label in the crystal structure. Perhaps the suspected flexibility of this helix brings it into proximity of the label for some conformational states of the complex.

Modeling of MS/C-Ring Interface of the Bacterial Flagellar Motor

The $FliF_C$:$FliG_N$ complex was then docked into 3D cryo-EM reconstructions of the intact CW locked *Salmonella* motors (Thomas

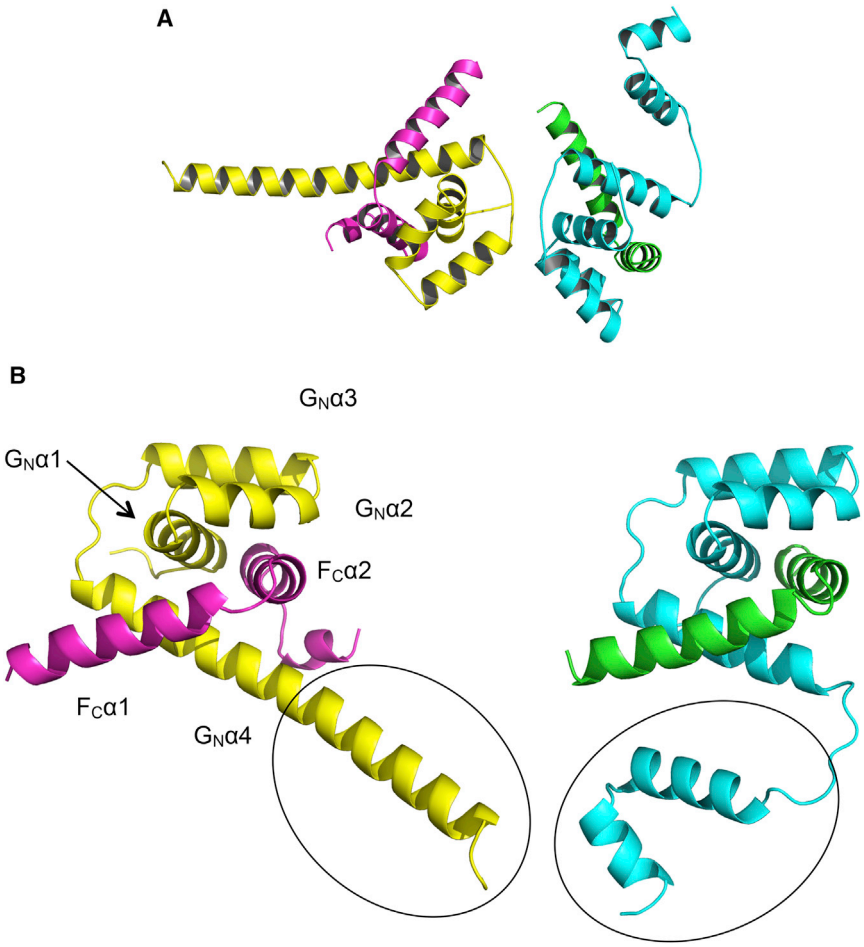

Figure 3. Crystal Structure of $FliF_C$:$FliG_N$
The two unique heterodimers per asymmetric unit oriented as in the crystal (A) or with the same perspective (B) ($FliF_C$, violet and green; $FliG_N$, yellow and cyan). The two different morphologies of the terminal $FliG_N$ helix are circled. See also Figures S3 and S5–S7.

et al., 2006). It was assumed that the $FliF_C$ peptide descends perpendicular to the inner membrane, despite the 32-residue gap present between $F_C\alpha1$ and the second transmembrane helix (TM2) region of $FliF_{NM}$. Symmetric rings were generated that contained either 24, 25, or 26 copies of $FliF_C$:$FliG_N$, consistent with previously determined FliF:FliG stoichiometry (Thomas et al., 2006). When $FliF_C$:$FliG_N$ rings with 24 or 26 subunits were docked into the C_{25} cryo-EM density, there were either clashes from overlapping secondary structural motifs (26 subunits) or unaccounted areas of electron density (24 subunits). Rings modeled with C_{25} symmetry had minimal steric clashes, minimized areas of unassigned density, and produced a correlation coefficient of 0.83 at 30 Å resolution (Figures 5A and 5B). Thus, the dimensions of the $FliG_N$:$FliG_C$ complex agree well with the MS/C-ring symmetry. In modeling the MS/C-ring interface, $F_C\alpha1$ was directed upward toward the inner membrane, an orientation that conferred biological relevance and allowed for systematic packing of all 25 subunits within minimal steric clashes (Figures 5A and 5B). In agreement with the model, recent bioinformatics-based modeling of the upper periplasmic region of $FliF_{NM}$ indicates 25 FliF subunits per MS ring (Bergeron, 2016).

In an effort to extend the modeling further, we carried out the same fitting technique with a $FliG_{MC}$:$FliM_M$ complex structure previously generated via X-ray crystallography and pulse-dipolar electron spin resonance (PDB: 4QRM, Sircar et al., 2015). In total, 34 copies of a single $FliG_{MC}$:$FliM_M$ complex were fit into the rotor density, producing a correlation coefficient of 0.79 (Figure 5B). Notably, there remains a disparity between the $FliG_{MC}$ and $FliG_N$ stoichiometry by nine copies. This symmetry mismatch is well recognized (Thomas et al., 1999, 2001; Manson, 2007; Berg, 2003; Sowa and Berry, 2008), and could result from unoccupied positions of $FliG_{MC}$ in the C ring (Sircar et al., 2015), non-equivalence in the FliG:FliM contacts (Paul et al., 2011; Sarkar et al., 2010) or as a result of adaptive remodeling of both FliM and FliN (Fukuoka et al., 2010; Lele et al., 2012; Delalez et al., 2014). Nonetheless, the current model suggests that 34 copies of FiG_N could not fit within the upper portion of the EM density.

Functional Analysis of the $FliF_C$:$FliG_N$ Complex

To validate the structure of $FliF_C$:$FliG_N$, site-directed mutants were evaluated by in vivo motility assays. All experiments were performed in *E. coli* with homologous *E. coli* proteins, where FliF and FliG share 29% and 36% sequence similarity with the *T. maritima* proteins, respectively, and conserve nearly all of the key residues involved in the complex interface (Figure S7) (Levenson et al., 2012; Thomas et al., 2001). In addition, residue substitutions at the FliF-FliG interface were tested in protein interaction studies and crosslinking of engineered cysteine mutants were further employed to probe the functional FliF:FliG interface.

Hydrophobic to aspartate residue substitutions in FliG were made, and cell migration rates were measured relative to wild-type (Figures 6A and 6B). Residue substitutions along the FliF:-FliG interface observed in the crystal structure proved most detrimental to motility. Specifically, motility defects were strongest for changes that are in close proximity to $F_C\alpha2$, especially at positions Leu13, Leu29, Leu37, Ile17 (*E. coli* numbering), which is consistent with the interactions between $FliF_C$ and FliG found in the crystal structure.

Analysis with the bacterial adenylate cyclase two-hybrid (BACTH) method provided independent support for a strong FliF:FliG interaction involving the interfaces observed in the crystal structure (Figure 6D) (Miller, 1972; Karimova et al., 2001; Battesti and Bouveret, 2012). BACTH experiments used hybrid constructs containing the $FliF_C$ (*E. coli* residues 505–552) and $FliG_N$ (*E. coli* residues 1–87). In experiments with wild-type $FliF_C$ and

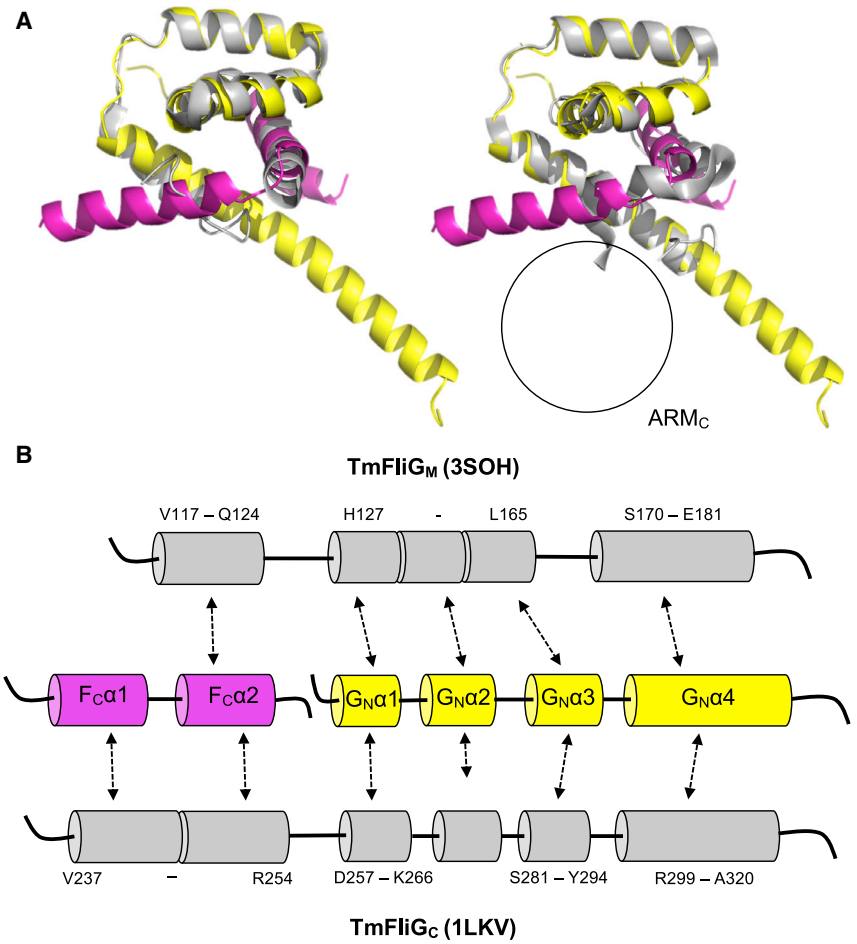

Figure 4. Domain Repeats within FliG

(A) Superimposition of *T. maritima* $FliF_C$:$FliG_N$ complex ($FliF_C$, violet; $FliG_N$, yellow) and *Thermotoga maritima* (left) $FliG_M$ (gray, PDB: 3SOH, RMS 1.053 Å, 40 residues) and (right) $FliG_C$ (gray, PDB: 1LKV, RMS 1.227 Å, 63 residues). The black circle signifies the absence of a corresponding ARM_C domain.

(B) Comparison of secondary structure motifs and primary sequence alignment of the superimposed regions.

See also Figure S4.

$FliG_N$, strong color development was observed on MacConkey plates, and measurements of β-galactosidase activity afforded values comparable with the leucine-zipper positive control (Figure 6C). Hydrophobic to aspartate replacements of FliG on the predicted interface weakened the interaction in a pattern similar to the motility phenotypes. Residue substitutions made to FliF provided similar validation of the expected contact sites (Figure S8). These results suggest that the interface involving $F_C\alpha2$ may be chiefly responsible for the strength of the interaction. Consistent with this, a hydrophobic to aspartate replacement at FliF residue 542 in $F_C\alpha2$ eliminated both motility and the two-hybrid interaction. A mutation at position Val538 in $F_C\alpha1$ caused a significant reduction in migration rate, while not diminishing the FliF:FliG interaction. In liquid culture, this mutant exhibited relatively weak motility and a substantial fraction of immotile cells, indicating a delay or partial defect in flagellar assembly. Thus, the V538D replacement alters the FliF:FliG relationship while not greatly weakening the interaction.

To further probe the FliF:FliG interaction in vivo, crosslinking of engineered cysteine mutants were employed to map the binding site interface between FliF and FliG in *E. coli.* Targeted disulfide crosslinking experiments indicate that the FliF:FliG relationship in *E. coli* is similar to that observed in the structure of the *T. maritima* proteins (Figure 7C). Fifty-five double-cysteine mutants were made (Figure 7A; Table S3). In total, seven relatively strong crosslinks were observed, all involving positions that are in proximity in the crystal structure (C_β-C_β distances 6–10.5 Å). All the cysteine double mutants that displayed strong crosslinking retained significant function (45%–85% of wild-type) in soft agar. Crosslinking experiments yielded one surprising result: Cys543 in FliF showed only weak crosslinking although this position is predicted to be close to several of the $FliG_N$ cysteine replacements. The strongest crosslink of Cys543 (still weak in absolute terms) was to Cys29 in FliG, which according to the structure is the closest (to 543) of the 11 FliG replacements examined. Residue 543, normally Ile, resides in $F_C\alpha1$ and is buried at the FliG:FliF interface. We hypothesized that packing in this region might be so stable as to prevent deprotonation or necessary movements of the buried cysteine side chains for crosslinking. In an attempt to loosen the interface and increase the reactivity of Cys543, the adjacent Arg544 was replaced with alanine; however, crosslinking was not significantly increased. Crosslinking was then carried out in the presence of urea (Figure 7B). The crosslink to FliG at Cys29 was slightly enhanced in the presence of 3 M urea, while crosslinking to a more distant position (Cys44) remained negligible.

Overall, results from the in vivo experiments fit well with the crystallographic structure of the $FliF_C$:$FliG_N$ complex, and indicate that the FliF:FliG interfaces are essentially identical in *E. coli* and *T. maritima*. As expected, the FliF:FliG interaction is critical for function. Mutant phenotypes and the non-reactivity of Cys543 highlight the importance of the interactions involving $F_C\alpha2$ and indicate that packing at this interface may be unusually stable.

DISCUSSION

The MS/C-ring interface is an essential contact site of the flagellar motor. Not only does it serve as a checkpoint during flagellar morphogenesis but it also positions FliG with respect to the inner membrane such that it can (1) bind to the MS ring to propagate rotation, (2) interact with the stator complexes to confer torque generation to the switch complex, and (3) position

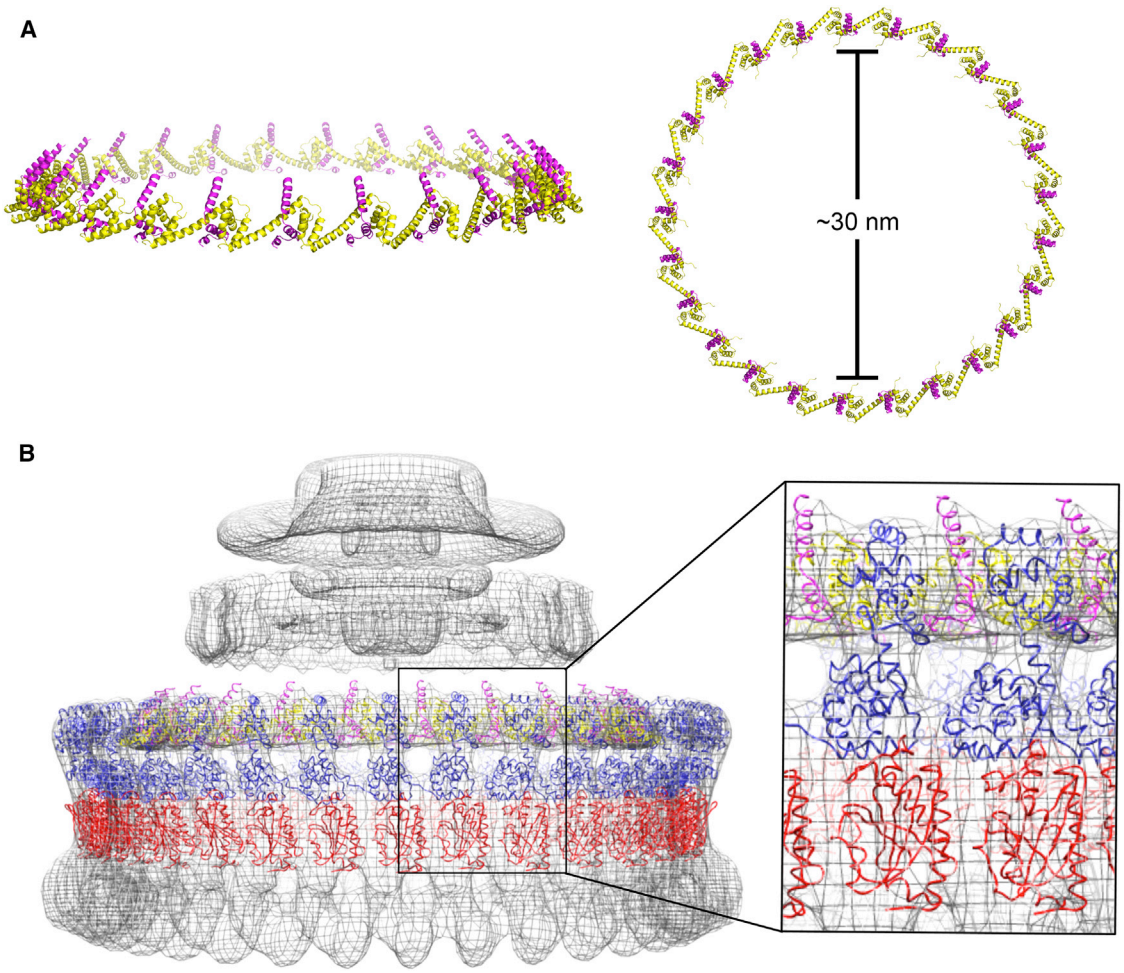

Figure 5. Modeling of the $FliF_C$:$FliG_N$ Ring with C_{25} Symmetry

(A) Fully assembled $(FliF_C:FliG_N)_n$ ring (n = 25 copies) showing the side (left) and top (right) view.

(B) $(FliF_C:FiG_N)_{25}$ ring and $(FliM_M:FliG_{MC})_{34}$ ring (red, $FliM_M$; blue, $FliG_{MC}$) superimposed with the EM density of the *Salmonella* rotor (Thomas et al., 2006) Ring density simulated at a 30 Å from the structures gave correlation coefficients with the EM density as follows: $FliF_C$:$FliG_N$, 0.83; $FliM_M$:$FliG_{MC}$, 0.79.

FliG such that it can bind to FliM to anchor CW/CCW switching and rotor dynamics (Berg, 2003; Sowa and Berry, 2008). Although fusion-deletion and mutagenesis studies have established that FliF and FliG interact through their N- and C-terminal domains, respectively, a molecular level view of this interaction remained elusive. The 2.1 Å resolution crystal structure of $FliF_C$:$FliG_N$ defines the interface between the MS and C rings within the flagellar motor. Furthermore, by reconciling the $FliF_C$:$FliG_N$ crystal structure with NMR, SAXS, in vivo assays, and modeling to cryo-EM reconstructions, we validate the structure as biologically relevant and further expand current understanding of protein organization at the MS/C-ring interface.

Fusion of the $FliF_C$ peptide to $FliG_N$ was an effective strategy for producing the complex. Comparing TROSY-HSQC ^{1}H-^{15}N NMR spectroscopy of the fused protein to the complex formed by its components indicates that the fusion folds as the native complex (Figure 2). Given the intimate contact formed by the two separate proteins, it is not surprising that they appear to fold as one unit. Notably, the ability of the cleaved and non-cleaved moieties to form essentially the same structure places spatial restrictions on the location of the $FliF_C$ binding site. Fortunately, these restrictions were satisfied in the native $FliF_C$:$FliG_N$ complex (Figure 3) and found to be in agreement with the $FliF_C$:$FliG_N$ interface mapped from the PRE studies (Figure S6; Table S2).

$FliF_C$:$FliG_N$ crystallizes in two conformations (Figure 3A). It was important to consider both when modeling the MS/C-ring interface. The $FliG_N$ core that houses the $FliF_C$ binding site remains invariant, owing to the strength of the FliF:FliG interaction. However, the C-terminal tail of $FliG_N$ ($G_N\alpha4$) assumes either an extended α helix or three segmented helices (Figure 3B). Although the crystal lattice may influence these conformations, the solution-state complex favors the extended helix (Figures S3B and S3C). Nonetheless, the more compact conformation may play a role in motor operation, as it confers a higher degree of flexibility and thus could serve as a flexible hinge to absorb stress during rotation reversals. Modeling of the $FliF_C$:$FliG_N$ structure into the ring density (Figures 5A and 5B) directs $F_C\alpha1$

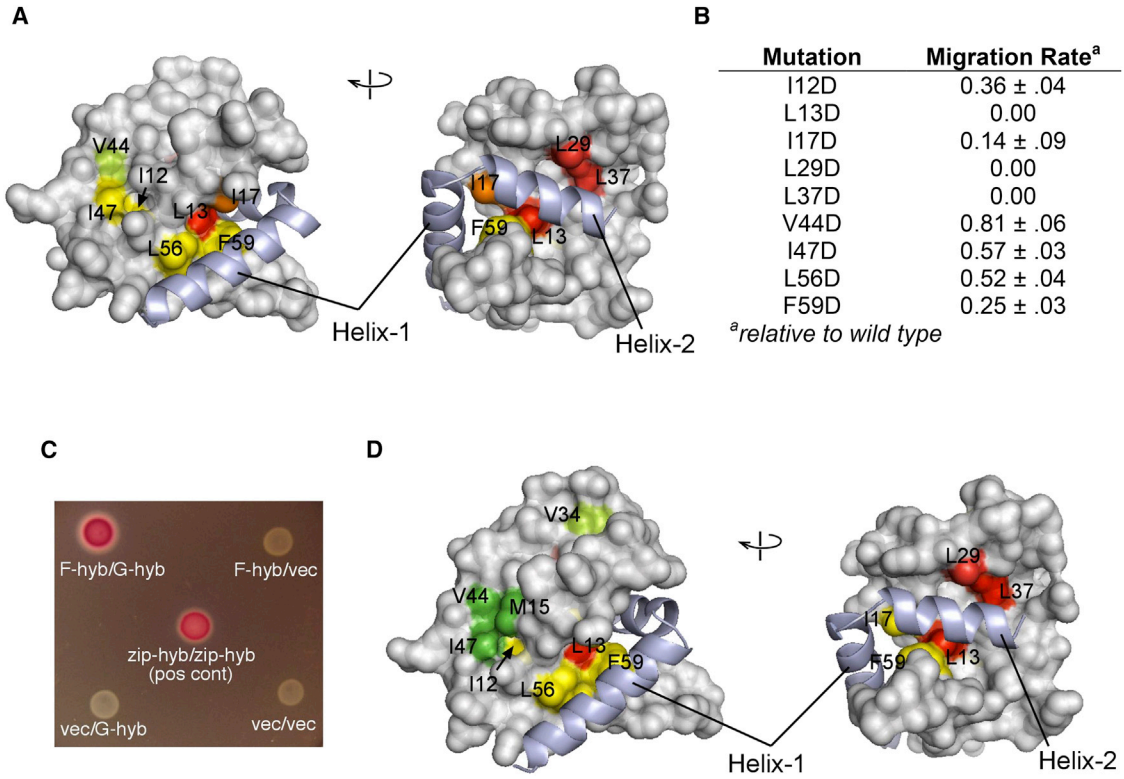

Figure 6. In Vivo *E. coli* Motility and Interaction Assays

(A) Two views of the $FliG_N$ domain, showing motility defects that result upon replacement of the indicated hydrophobic residues with aspartate. Motility phenotypes were tested by expressing mutant FliG proteins in the fliG null strain. Yellow-green, rate less than 100% but greater than 70% of wild-type; yellow, rate between 20% and 70% of wild-type; orange, motile but at less than 20% of wild-type; red, immotile.

(B) A table summarizing the relative rates, values are the mean ± SD for three determinations.

(C) Interaction between $FliF_C$ (residues 505–552) and $FliG_N$ (residues 1–87) observed in the bacterial adenylate cyclase two-hybrid system. Positive interactions drive expression of β-galactosidase. Negative controls and a leucine-zipper positive control are shown.

(D) Effects of hydrophobic-to-aspartate replacements in $FliG_N$ on the FliF-FliG interaction. Coloring is based on β-galactosidase activities: Green, activity indistinguishable from wild-type; yellow-green, activity less than 100% but greater than 70% of wild-type; yellow, activity between 20% and 70% of wild-type; red, activity decreased to the level of negative controls. $FliF_C$ shown light purple in all figures.

See also Figure S8.

toward the inner membrane of TM2 of FliF. The 32 unaccounted residues between $FliF_C$ $F_C\alpha2$ and TM2 of $FliF_{NM}$ could similarly serve as a flexible hinge.

Importantly, $FliG_N$ requires $FliF_C$ to fold into a stable $FliG_M$/$FliG_C$-like domain, and thus the stoichiometry of FliF to FliG is most likely to be 1:1. Such a 1:1 complex has important implications for the overall structure of the rotor, as FliG must interact with FliM, of which there are ~34 copies. Therefore, either not every FliM interacts with one FliG in the same way or the protein stoichiometry in the MS and C rings are not correct. The latter seems unlikely, as 25 copies of the FliF:FliG complex fit well around the upper switch, and it is difficult to accommodate more subunits without substantial steric clashes. Further, the current finding that the MS/C-ring interface has C_{25} symmetry is in agreement with recent homology modeling of the periplasmic region of FliF (Bergeron, 2016).

FliG is divided into three distinct domains, where each domain has evolved to carry out a specific function within the flagellar switch (Lloyd et al., 1996; Lloyd and Blair, 1997; Berg, 2003; Sowa and Berry, 2008). $FliG_N$ contains the binding site for $FliF_C$ and anchors the C ring to the inner membrane, $FliG_M$ interacts with $FliG_C$ and $FliM_M$ to propagate CCW/CW switching, and $FliG_C$ contains conserved charged residues to interact with membrane-bound stators in torque generation (Lloyd et al., 1996; Lloyd and Blair, 1997; Berg, 2003; Sowa and Berry, 2008). The structure of FliG determined from *A. aeolicus* agrees with structures of the M- and C-terminal domains (Brown et al., 2002; Paul et al., 2011). A notable feature of unbound $FliG_N$ identified in the full-length structure was the structural similarity between $AqFliG_N$ helices N1-4 and $AqFliG_C$ terminal helices 3–6 (Lee et al., 2010). A similar observation was made previously from the crystal structure of $FliG_{MC}$ from *T. maritima* (PDB: 1LKV) regarding the ARM motifs present in $FliG_M$ and $FliG_C$ ($ARM_{M/C}$) (Brown et al., 2002). Interestingly, the $FliF_C$:$FliG_N$ complex shows how structural replication within $FliG_C$ is even more extensive than in $FliG_{MC}$ (Figures 4 and S4). When FliF is bound to FliG, all three domains adopt similar conformations such that FliF:FliG aligns well with the ARM_M motif and $helix_{MC/NM}$ in $FliG_M$, as well as with helices 1–6 in $FliG_C$. The striking similarity of the FliF:FliG fold with that of $FliG_M$ and $FliG_C$ suggests

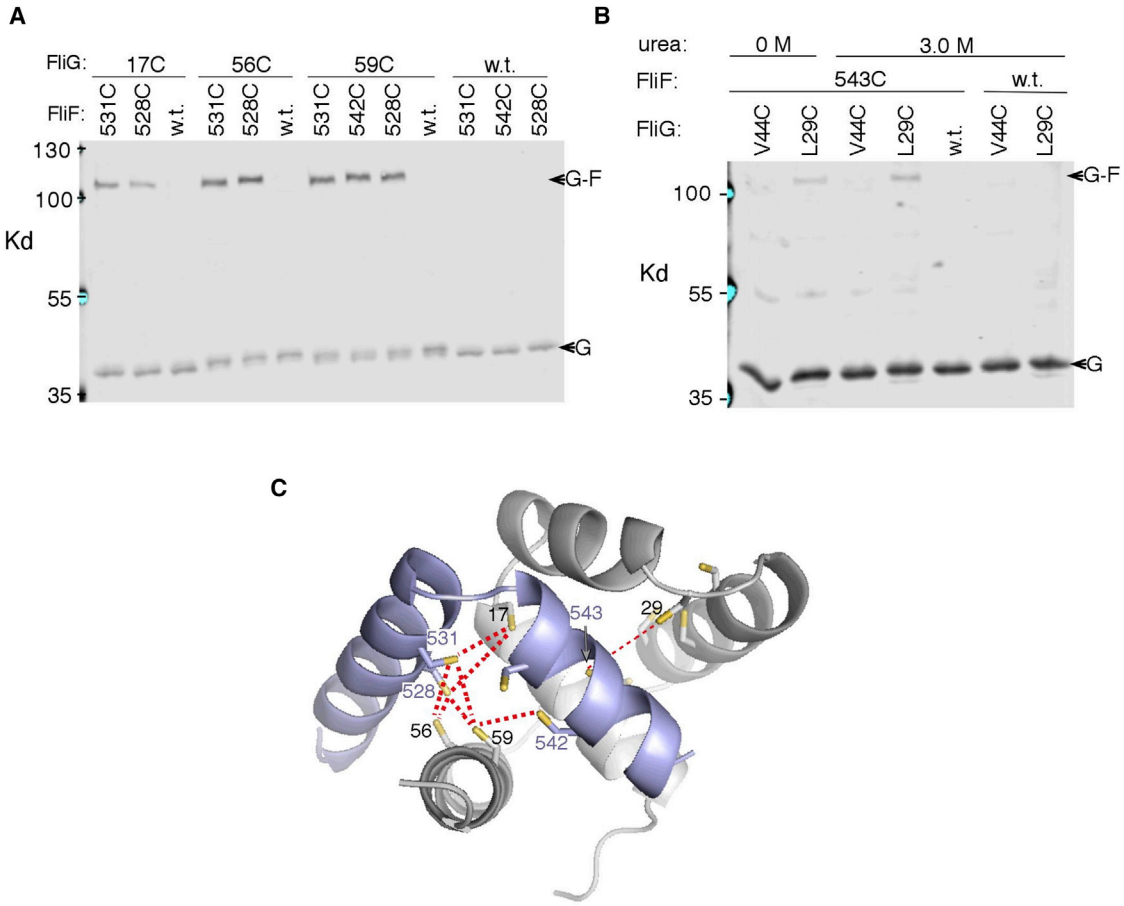

Figure 7. In Vivo FliG-FliF Crosslinking

(A) Products of iodine-induced disulfide crosslinking were detected using anti-FliG immunoblots. The seven cysteine pairs that gave strong crosslinking are shown together with single cysteine controls. Crosslinking was weak or undetectable for 48 other cysteine pairs tested (Table S3). In addition to the indicated cys-mutant FliF, a comparable amount of wild-type FliF (expressed from the chromosome) was present in the crosslinking experiments; thus, crosslinking yields should underestimate what would occur if all of the FliF carried the Cys replacement.

(B) A low-yield crosslink between FliG position 543 and FliG position 29 that is made somewhat stronger (by ~50%) in the presence of 3 M urea. The more distant position Cys44 did not crosslink.

(C) Mapping the crosslinks onto the FliG-FliF structure. Thicker red lines indicate the crosslinks observed under standard conditions, and the thin red line indicates the weaker, urea-enhanced crosslink involving the buried position 543.

See also Figure S8.

domain shuffling may relate all three of the FliG domains (Di Roberto and Peisajovich, 2014). Either the N-terminal helix of $FliG_N$ was transferred to the C terminus of FliF or the $FliG_N$:$FliF_C$ unit was fused and propagated to generate $FliG_M$ and $FliG_C$. The genes for FliF and FliG are often adjacent, in the same orientation, and expressed from the same promoter. Thus, in many instances the coding sequences for the two helices that complete the $FliG_N$ superhelix are tightly coupled to the FliG gene. Furthermore, in *Chlamydia* the C-terminal region of FliF has been replaced with an entire $FliG_M$-like domain (Bergeron, 2016). Thus, the interface between the FliF TM2 and the C ring is always a $FliG_M$-like domain, whether it is composed of a single polypeptide or two that mate $FliF_C$ to $FliG_N$. Interestingly, upon comparing the sequences of the $FliF_C$:$FliG_N$ complex with $FliG_M$, the region where $FliF_C$ terminates and $FliG_N$ begins coincides with the $FliM_M$-binding EHPQR motif of $FliG_M$ (Paul et al., 2011; Vartanian et al., 2012) (Figure 4B). If $FliG_M$ and $FliF_C$:$FliG_N$ share a common origin, severing a continuous $FliG_N$ domain into two at a site that maps to the position on $FliG_M$ that binds to $FliM_M$ may have been advantageous to prevent incorrect binding of $FliG_N$ to $FliM_M$ during MS/C-ring assembly.

The contact residues of the FliF:FliG structure mediate protein interactions in cells and are critical for generating functional flagella. Substitution of key hydrophobic residues to aspartic acid along the FliF:FliG interface of both FliG (Figure 6A) and FliF (Figure S8) disrupt cell motility and protein interactions. Although $F_C\alpha1$ buries ~570 $Å^2$ of surface area, the functional specificity and strength of the FliF:FliG interaction can largely be attributed to $F_C\alpha2$. Disulfide crosslinking data provide direct biochemical evidence in support of these findings. One surprising observation was the relatively small extent of crosslink formation between buried FliF Cys543 and any potential disulfide partner (Figure 7B; Table S4). This result likely reflects the uniquely strong interaction between $F_C\alpha2$ and FliG that

prevents movement of the cysteine residues or access to oxidants. These results provide evidence for the conjecture that $FliF_C$ and $FliG_N$ essentially fold as one domain to provide a robust anchor for the C ring to the membrane. It is not surprising then that the FliF:FliG interaction is much stronger than that of the FliG:FliM or FliM:FliN and can persist longer at low pH without dissociation (Francis et al., 1994).

Overall, by combining data from X-ray crystallography, SAXS, NMR, modeling to cryo-EM structures, and in vivo functional studies, we have defined the FliF:FliG interaction at the MS/C-ring interface. The structure has then been elaborated into an updated model for the upper switch. Importantly, the structure suggests that the FliF:FliG stoichiometry is likely the same and that domain shuffling appears to have driven the association of these key building blocks of the flagellar motor. We propose a model where a domain is duplicated and then genetically split so that a folding unit can associate two otherwise non-interacting proteins with high affinity. It is notable that protein engineering has used a similar strategy of split protein complementation to effect interactions in cells through the development of tools such as split GFP, ubiquitin, and luciferase proteins (Xing et al., 2016).

EXPERIMENTAL PROCEDURES

Protein Expression and Purification

Native proteins were expressed in BL21 (DE3) *E. coli* cells, grown at 37°C in Luria-Bertani (LB) medium containing 50 μg/mL kanamycin, and induced with 1 mM isopropyl β-D-1-thiogalactopyranoside (IPTG) at 25°C after reaching an OD_{600} of ~0.6. Selenomethionine variants were expressed in B834 methionine auxotrophic *E. coli* cells at 37°C in minimal medium containing 100 μg/mL ampicillin hydrochloride and 50 mg/L ± L-selenomethionine.

All proteins were purified according to the following procedure: cell pellets were re-suspended in lysis buffer (25 mM HEPES [pH 7.5], 500 mM NaCl, 5 mM imidazole), lysed via sonication, and the lysate was then centrifuged at 20,000 rpm for 45 min at 4°C. The supernatant was passed through an Ni-NTA column, washed with 50 mL of wash buffer (25 mM HEPES [pH 7.5], 500 mM NaCl, 25 mM imidazole), and eluted with elution buffer (25 mM HEPES [pH 7.5], 500 mM NaCl, 200 mM imidazole). The linker between $FliG_N$ and $FliF_C$ was removed by overnight incubation with TEV protease at 30°C. TEV was removed via centrifugation, and the $FliF_C$:$FliG_N$ complex was dialyzed extensively against 50 mM sodium phosphate (pH 6.5). For the preparation of selenomethionine $FliF_C$:$FliG_N$, all buffers were supplemented with 10 mM DTT. Successful selenomethionine incorporation was confirmed via whole-protein positive ion electrospray liquid chromatography tandem mass spectrometry.

Crystallization, Data Collection, and Phasing

The $FliF_C$:$FliG_N$ complex was subjected to sparse course matrix screening in 600 nL drops at a protein concentration of 65 mg/mL. Crystals grew in 100 mM HEPES (pH 7.5), 25% (w/v) PEG 3000, 200 mM NaCl at 25°C after ~7 days. Selenomethionine-incorporated crystals grew from 33 mg/mL protein, 100 mM imidazole (pH 7.2), 130 mM NaCl, 30% (w/v) PEG 8000 in ~14 days.

Briefly, datasets were integrated and scaled in HKL2000 and SCALPACK (see Table 1). Phasing of the anomalous dataset was done with Phenix HYSS, and the model was built with Autobuild (Phenix) programs (Adams et al., 2010). Manual adjustments to the model were made with COOT, and subsequent refinements were carried out with Phenix Refine. The final $FliF_C$:$FliG_N$ model has an R_{free} of 21.74% and an R_{work} of 16.92% with excellent stereochemistry.

Ring Simulation and Fitting into Cryo-EM Maps

Low-resolution cryo-EM maps of whole rotor density containing the C, MS, L, and P rings were provided by Thomas et al. (2006). To construct a model of the upper C-ring/MS-ring interface, a single $FliF_C$:$FliG_N$ complex was aligned to the whole rotor density such that the coordinate systems of the crystal structure PDB file coincided with that of the rotor MRC map file. The center of mass was calculated for the placed complex, and the structure was duplicated n times and rotated 360/n degrees around an axis chosen perpendicular to the membrane. The ring was simulated to a radius of 15 nm, a distance corresponding to the radius of the EM map. Three rings of n = 24, 25, and 26 C_n fold symmetry were generated and evaluated with respect to the EM density. By inspection, only rings of C_{25} fold symmetry produced a clash-free model that has minimal gaps in density. The C_{25} upper C/MS-ring model was fit into the EM map using the Fit to Map program in Chimera. When simulating the EM map to a resolution of 30 Å, the C_{25} fold $FliF_C$:$FliG_N$ ring provided good agreement with the whole rotor density and produced a correlation coefficient of 0.83. The above procedure was repeated with an $FliG_{MC}$:$FliM_M$ model (PDB: 4QRM), to give a mid rotor subunit copy number of 34 and a correlation coefficient of 0.79.

Generation, Purification, and NMR Analysis of Isotopically Enriched $FliF_C$:$FliG_N$ Complex

The fusion $FliF_C$(495–532):$FliG_N$(1–102) construct was generated by traditional molecular cloning methods. The $FliF_C$ portion was amplified from a plasmid obtained from the JCSG and cloned into a plasmid containing $FliG_N$(1–102) (Levenson et al., 2012). All NMR data were collected with a construct similar to Figure S1, however, the construct only included one TEV protease site between the His_8 tag and the $FliG_N$ domain. Isotopically labeled proteins were grown in M9 minimal medium supplemented with $^{15}NH_4Cl$, ^{13}C glucose, and/or D_2O (when necessary). Rosetta (DE3) *E. coli* cells were used for expression of all constructs. Cells were grown at 37°C, and upon reaching an OD_{600} of ~0.6, were induced with a final concentration of 1 mM IPTG and expressed for approximately 6 hr. Purification was identical as described previously. After SEC, the protein samples were dialyzed into 50 mM sodium phosphate, 100 mM NaCl (pH 6.5) for NMR analysis. After dialysis, all samples were concentrated to their final concentration, at which point 0.02% (w/v) NaN_3 was added. NMR spectra were collected on a Bruker Avance 800 MHz spectrometer equipped with a cryoprobe.

E. coli Strains and Media for Interaction and Motility Studies

Escherichia coli strains and plasmids are listed in Table S1. All strains were derivatives of the wild-type strain RP437. Chromosomal in-frame deletions or point mutations were made by using the lambda red method (Datsenko and Wanner, 2000). TB medium contained (per liter) 10 g of tryptone and 5 g of NaCl; LB medium contained the same plus 5 g of yeast extract. Soft-agar motility plates used TB medium and Bacto-agar at 2.6 g/L. Ampicillin was used at 100 μg/mL in liquid medium, 100 μg/mL in selective plates, and 50 μg/mL in soft-agar motility plates. Chloramphenicol was used at 50 μg/mL in liquid medium and selective plates and at 25 μg/mL in motility plates. IPTG and sodium salicylate were prepared as aqueous 0.1 M and 10 mM stocks and used at the concentrations indicated in the figures.

Motility Assay

All of the experiments examining motility defects were carried out in the respective null backgrounds (DB225, EKS10, see Table S1). Soft-agar plates were spotted with 3 μL of overnight cultures. Once migration began, colony size was measured at regular intervals, and plots of diameter versus time were fitted to a line to determine rates. Rates are reported relative to wild-type controls measured in the same experiment. Effects of Asp replacements on motility were measured in strains expressing the mutant FliG from a plasmid (derivatives of pKP619), induced with 100 μM IPTG. Effects of Asp replacements in FliF were measured in strains expressing FliF from the plasmid pEK16, induced with 0.3 μM salicylate, and additionally expressing wild-type FliG from plasmid pKP619 (induced as above), in a Δ*fliF* strain. The additional, plasmid-expressed FliG was found to be necessary for optimal function. Effects on motility of cysteine replacements in FliG and FliF were measured in a Δ*fliFfliG* double-deletion strain, with both proteins expressed from plasmids.

In Vivo and Crosslinking Mutagenesis

Site-directed mutations were made using the QuikChange method (Stratagene). DNA sequencing and oligonucleotide synthesis were carried out by core facilities at the University of Utah.

Double-Cysteine Crosslinking

Disulfide crosslinking between FliF and FliG was studied in strains expressing cysteine-containing FliG variants from the chromosome and cysteine-containing FliF variants from plasmid pEK16. For these experiments, wild-type protein (FliF) was present along with the Cys-mutant FliF. Levels of the two were roughly equal. The plasmid was induced with 0.2 μM salicylate, which gave FliF levels sufficient to compete with the wild-type (cysteine-less) FliF expressed from the chromosome but not so high as to impair motility. (Motility impairment occurred with induction by 1 μM or higher.) Cells were cultured overnight at 37°C and diluted 100-fold into TB containing antibiotic and 0.2 μM sodium salicylate then grown at 32°C for 5–6 hr (to OD_{600} 0.7–0.8). OD_{600} was measured to adjust the cell density, then equal numbers of cells were pelleted and re-suspended with XL buffer (20 mM Na-phosphate (pH 7.4), 150 mM NaCl). For crosslinking with iodine, 0.1 mL of cell mixed with 4 μL of 25 mM iodine for 3 min at room temperature, then sulfhydryl groups were blocked by addition of 2 μL of 0.5 M NEM and incubation at room temperature for 3 min. Samples were mixed with an equal volume of 2× non-reducing loading buffer and heated at 95°C for 10 min before loading on SDS-PAGE gels. Some experiments included urea during the crosslinking step at the concentrations indicated in the figures to test the effects of partially destabilizing the proteins.

SDS-PAGE and Immunoblotting

Proteins were resolved in 7.5% SDS-PAGE gels and transferred onto nitrocellulose using a Transblot turbo apparatus (Bio-Rad). Rabbit polyclonal antibody against FliG was used at 1:1,000 dilution in a solution containing PBS (pH 7.4), 0.1% gelatin, and 0.01% sodium azide. Immunoblots were visualized and analyzed using the LiCor Odyssey infrared imaging system.

Two-Hybrid Interaction Assay

BACTH measurements of the FliF:FliG interaction used vectors provided in a kit from Euromedex, following previously published procedures (Miller, 1972; Battesti and Bouveret, 2012) with minor modifications. Cells from a single colony were grown overnight at 32°C in LB containing ampicillin and 0.5 mM IPTG, then pelleted and re-suspended in PBS buffer; 0.04 mL of cells were mixed with 0.96 mL of Z buffer (0.06 M Na_2HPO_4, 0.04 M NaH_2PO_4, 0.01 M KCl, 0.001 M $MgSO_4$ [pH 7.0], 0.08% SDS, 0.22% [v/v] β-mercaptoethanol). Cells were permeabilized by addition 100 μL of chloroform and vortexed for 10 s, followed by incubation at 30°C for 5 min. Reaction was started by adding 0.2 mL of ortho-nitrophenyl-β-galactoside solution (4 mg/mL). After measured times of reaction at 30°C, the reaction was stopped by addition of 0.5 mL of 1 M $NaHCO_3$. Product was quantified by measurement of OD_{420}, with a correction due to cell scattering. Activity in Miller units was computed according to the formula: $(1{,}000 \times [OD_{420} - 1.75 \times OD_{550}])/(\text{time of reaction} \times \text{volume of culture used} \times OD_{600})$, where OD_{420} and OD_{550} are read from the reaction mixture and OD_{600} reflects cell density in the washed cell suspension.

ACCESSION NUMBERS

$FliF_C$:$FliG_N$ complex PDB: 5TDY; $FliF_C$:$FliG_N$ NMR assignments BMRB: 26908.

SUPPLEMENTAL INFORMATION

Supplemental Information includes Supplemental Experimental Procedures, eight figures, and four tables and can be found with this article online at http://dx.doi.org/10.1016/j.str.2016.12.006.

AUTHOR CONTRIBUTIONS

Conceptualization: B.R.C., F.W.D., D.F.B.; Methodology, R.L., M.J.L.; Investigation: M.J.L., R.L., E.K., and R.S.; Writing – Original Draft: M.J.L. and B.R.C. In Vivo Data/Discussion: E.K. and D.F.B., NMR Data/Discussion: R.L. and F.W.D.; Writing – Review & Editing: M.J.L., R.L., B.R.C., F.W.D., D.F.B., and R.S.; Funding Acquisition, Resources, and Supervision: B.R.C., F.W.D., and D.F.B.

ACKNOWLEDGMENTS

Research reported in this publication was supported by the NIGMS of the NIH under Award Numbers R01GM064664 (D.F.B., B.R.C.), T32GM008500 (M.J.L., B.R.C.) and R01GM59544 (F.W.D.). The content is solely the responsibility of the authors and does not necessarily represent the official views of the NIH. We thank NECAT (NIH grant P41 GM103403) and CHESS/MacCHESS (NSF: DMR-1332208; NIH: P41 GM-103485) for access to data collection facilities.

Received: October 5, 2016
Revised: November 21, 2016
Accepted: December 12, 2016
Published: January 12, 2017

REFERENCES

Adams, P.D., Afonine, P.V., Bunkóczi, G., Chen, V.B., Davis, I.W., Echols, N., Headd, J.J., Hung, L.-W., Kapral, G.J., Grosse-Kunstleve, R.W., et al. (2010). PHENIX: a comprehensive Python-based system for macromolecular structure solution. Acta Crystallogr. *D66*, 213–221.

Andrade, M.A., Petosa, C., O'Donoghue, S.I., Muller, C.W., and Bork, P. (2001). Comparison of ARM and HEAT protein repeats. Structure *309*, 1–18.

Battesti, A., and Bouveret, E. (2012). The bacterial two-hybrid system based on adenylate cyclase reconstitution in *Escherichia coli*. Methods *5894*, 325–334.

Berg, H.C. (2003). The rotary motion of the bacterial flagella. Annu. Rev. Biochem. *72*, 19–54.

Bergeron, J.R. (2016). Structural modeling of the flagellum MS ring protein FliF reveals similarities to the type III secretion system and sporulation complex. PeerJ *4*, e1718.

Brown, P.N., Hill, C.P., and Blair, D.F. (2002). Crystal structure of the middle and C-terminal domains of the flagellar rotor protein FliG. EMBO J. *21*, 3225–3234.

Chen, S., Beeby, M., Murphy, G.E., Leadbetter, J.R., Hendrixson, D.R., Briegel, A., and Jensen, G.J. (2011). Structural diversity of bacterial flagellar motors. EMBO J. *30*, 2972–2981.

Chevance, F.F.V., and Hughes, K.T. (2008). Coordinating assembly of a bacterial macromolecular machine. Nat. Rev. Microbiol. *6*, 455–465.

Datsenko, K.A., and Wanner, B.L. (2000). One-step inactivation of chromosomal genes in *Escherichia coli* K-12 using PCR products. Proc. Natl. Acad. Sci. USA *97*, 6640–6645.

Delalez, N.J., Berry, R.M., and Armitage, J.P. (2014). Stoichiometry and turnover of the bacterial flagellar switch protein FliN. MBio *5*, e01216.

Di Roberto, R.B., and Peisajovich, S.G. (2014). The role of domain shuffling in the evolution of signaling networks. J. Exp. Zool. B Mol. Dev. Evol. *322*, 65–72.

Francis, N.R., Irikura, V.M., Yamaguchi, S., DeRosier, D.J., and Macnab, R.M. (1992). Localization of the *Salmonella typhimurium* flagellar switch protein FliG to the cytoplasmic M-ring face of the basal body. Proc. Natl. Acad. Sci. USA *89*, 6304–6308.

Francis, N.R., Sosinsky, G.E., Thomas, D., and DeRosier, D.J. (1994). Isolation, characterization and structure of bacterial flagellar motors containing the switch complex. J. Mol. Biol. *235*, 1261–1270.

Fukuoka, H., Inoue, Y., Terasawa, S., Takahashi, H., and Ishijima, A. (2010). Exchange of rotor components in functioning bacterial flagellar motor. Biochem. Biophys. Res. Commun. *394*, 130–135.

Grünenfelder, B., Gehrig, S., and Jenal, U. (2003). Role of the cytoplasmic C terminus of the FliF motor protein in flagellar assembly and rotation. J. Bacteriol. *185*, 1624–1633.

Hattori, M., Tanaka, Y., Fukai, S., Ishitani, R., and Nureki, O. (2007). Crystal structure of the MgtE Mg2+ transporter. Nature *448*, 1072–1076.

Karimova, G., Ullmann, A., and Ladant, D. (2001). Protein-protein interaction between *Bacillus stearothermophilus* tyrosyl-tRNA synthetase subdomains revealed by a bacterial two-hybrid system. J. Mol. Microb. Biotechnol. *3*, 73–82.

Lam, K.H., Lam, W.W., Wong, J.Y., Chan, L.C., Kotaka, M., Ling, T.K., Jin, D.Y., Ottemann, K.M., and Au, S.W. (2013). Structural basis of FliG-FliM interaction in *Helicobacter pylori*. Mol. Microbiol. *88*, 798–812.

Lee, L.K., Ginsburg, M.A., Crovace, C., Donohoe, M., and Stock, D. (2010). Structure of the torque ring of the flagellar motor and the molecular basis for rotational switching. Nature *466*, 996–1000.

Lele, P.P., Branch, R.W., Nathan, V.S.J., and Berg, H.C. (2012). Mechanism for adaptive remodeling of the bacterial flagellar switch. Proc. Natl. Acad. Sci. USA *109*, 20018–20022.

Levenson, R., Zhou, H., and Dahlquist, F.W. (2012). Structural insights into the interaction between the bacterial flagellar motor proteins FliF and FliG. Biochemistry *51*, 5052–5060.

Lipfert, J., and Doniach, S. (2007). Small-angle x-ray scattering from RNA, proteins, and protein complexes. Annu. Rev. Biophys. Biomol. Struct. *36*, 307–327.

Lloyd, S.A., and Blair, D.F. (1997). Charged residues of the rotor protein FliG essential for torque generation in the flagellar motor of *Escherichia coli*. J. Mol. Biol. *266*, 733–744.

Lloyd, S.A., Tang, H., Wang, X., Billings, S., and Blair, D.F. (1996). Torque generation in the flagellar motor of *Escherichia coli*: evidence of a direct role for FliG but not for FliM or FliN. J. Bacteriol. *178*, 223–231.

Macnab, R.M. (2003). How bacteria assemble flagella. Annu. Rev. Microbiol. *57*, 77–100.

Manson, M.D. (2007). How 34 pegs fit into 26 + 8 holes in the flagellar motor. J. Bacteriol. *189*, 291–293.

Miller, J.H. (1972). Experiments in Molecular Genetics: Assay of β-Galactosidase (Cold Spring Harbor Laboratory Press), pp. 352–355.

Minamino, T., and Imada, K. (2015). The bacterial flagellar motor and its structural diversity. Trends Microbiol. *23*, 267–274.

Minamino, T., Imada, K., and Namba, K. (2008). Molecular motors of the bacterial flagella. Curr. Opin. Struct. Biol. *18*, 693–701.

Minamino, T., Imada, K., Kinoshita, M., Nakamura, S., Morimoto, Y.V., and Namba, K. (2011). Structural insight into the rotational switching mechanism of the bacterial flagellar motor. PLoS Biol. *9*, e1000616.

Ogawa, R., Abe-Yoshizumi, R., Kishi, T., Homma, M., and Kojima, S. (2015). Interaction of the C-terminal tail of FliF with FliG from the Na+-driven flagellar motor of *Vibrio alginolyticus*. J. Bacteriol. *197*, 63–72.

Paul, K., Gonzalez-Bonet, G., Bilwes, A.M., Crane, B.R., and Blair, D. (2011). Architecture of the flagellar rotor. EMBO J. *30*, 2962–2971.

Sarkar, M.K., Paul, K., and Blair, D.F. (2010). Subunit organization and reversal-associated movements in the flagellar switch of *Escherichia coli*. J. Biol. Chem. *285*, 675–684.

Sircar, R., Borbat, P.P., Lynch, M.J., Bhatnagar, J., Beyersdorf, M.S., Halkides, C.J., and Crane, B.R. (2015). Assembly states of FliM and FliG within the flagellar switch complex. J. Mol. Biol. *427*, 867–886.

Sowa, Y., and Berry, R.M. (2008). Bacterial flagellar motor. Q. Rev. Biophys. *41*, 103–132.

Thomas, D.R., Morgan, D.G., and DeRosier, D.J. (1999). Rotational symmetry of the C ring and a mechanism for the flagellar rotary motor. Proc. Natl. Acad. Sci. USA *96*, 10134–10139.

Thomas, D., Morgan, D.G., and DeRosier, D.J. (2001). Structures of bacterial flagellar motors from two FliF-FliG gene fusion mutants. J. Bacteriol. *183*, 6404–6412.

Thomas, D.R., Francis, N.R., Xu, C., and DeRosier, D.J. (2006). The three-dimensional structure of the flagellar rotor from a clockwise-locked mutant of *Salmonella enterica* serovar Typhimurium. J. Bacteriol. *188*, 7039–7048.

Vartanian, A.S., Paz, A., Fortgang, E.A., Abramson, J., and Dahlquist, F.W. (2012). Structure of flagellar motor proteins in complex allows for insights into motor structure and switching. J. Biol. Chem. *287*, 35779–35783.

Xing, S., Wallmeroth, N., Berendzen, K.W., and Grefen, C. (2016). Techniques for the analysis of protein-protein interactions in vivo. Plant Physiol. *171*, 727–758.